

Redistributing Zn-ion flux by interlayer ion channels in Mg-Al layered double hydroxide-based artificial solid electrolyte interface for ultra-stable and dendrite-free Zn metal anodes

Yang Yang^a, Chaoyue Liu^b, Zeheng Lv^a, Hao Yang^c, Xian Cheng^a, Shengzhao Zhang^a, Minghui Ye^a, Yufei Zhang^a, Libao Chen^c, Jinbao Zhao^b, Cheng Chao Li^{a,*}

^a School of Chemical Engineering and Light Industry, Guangdong University of Technology, Guangzhou 510006, PR China

^b State Key Lab of Physical Chemistry of Solid Surfaces, State-Province Joint Engineering Laboratory for New Energy Vehicle, College of Chemistry and Chemical Engineering, Xiamen University, Xiamen 361005, PR China

^c State Key Laboratory for Powder Metallurgy, Central South University, Changsha 410083, PR China



ARTICLE INFO

Keywords:

Aqueous zinc-ion battery
Zn metal anode
Mg-Al layered double hydroxide
Artificial solid electrolyte interface
Zn-ion flux

ABSTRACT

The growth of Zn dendrites and self-corrosion reaction during electrochemical cycling is a long-standing issue impeding the practical application of zinc-ion batteries. Although various surface engineering strategies have shown great promise in suppressing zinc dendrites, the protective layers unavoidably hinder Zn²⁺ diffusion, resulting in increased internal impedance/polarization. Therefore, constructing smart interface protective layers with fast Zn²⁺ transfer kinetics is highly desirable but remains a key challenge. Here, an Mg-Al layered double hydroxide (LDH)-based artificial solid electrolyte interface (SEI) with Zn-ion diffusion channels is proposed. The well-aligned interlayer channels in the Mg-Al LDH skeleton is proved to efficiently engineer the distribution of Zn²⁺ ions and facilitate Zn²⁺ diffusion between the electrode/electrolyte interface, thus giving rise to stable Zn deposition. Moreover, the mechanically robust Mg-Al LDH artificial SEI acts as an interfacial layer to constrain H₂O-induced corrosion and hydrogen evolution reaction. Consequently, the Mg-Al LDH artificial SEI improves the Coulombic efficiency to 99.2% for more than 2000 cycles, and an ultralong lifespan of 1400 h has been achieved at 0.5 mA cm⁻². Notably, the zinc-ion capacitors by pairing the Zn@LDH anode and high-loading active carbon cathode deliver outstanding cycling stability with a high capacity retention of 93.7% up to 10000 cycles at the high areal current density of 37.5 mA cm⁻², portending the feasibility of practical applications.

1. Introduction

Lithium-ion batteries (LIBs) have revolutionized the electrochemical energy storage market over the past decade. [1] Nevertheless, due to the frequently occurred fire and even explosion accidents of LIBs in electric vehicles, mobile phones, and other electronic devices in recent years, the quest for exploiting alternative reliable battery technologies is increasingly aroused. Developing rechargeable aqueous battery system is regarded as a promising solution owing to its intrinsic nontoxicity, low production cost, high safety, and high ionic conductivity. [2] Among various aqueous battery technologies, aqueous zinc-ion batteries (ZIBs) have received tremendous attention owing to their advantages of high theoretical capacity (820 mAh g⁻¹) and appropriate redox potential (-0.76 V vs. standard hydrogen electrode). [3,4] Despite this broad potential, the practical application of aqueous ZIBs still faces challenges due

to dendrite formation of Zn metal anodes in mildly acidic electrolyte. [5]

According to the diffusion-controlled metal deposition model, the growth of metal dendrites is strongly influenced by the distribution of metal ions at the electrode/electrolyte interface. [6] Irregular Zn²⁺ ion concentration gradient will cause uneven and insufficient Zn²⁺ ion supply, and consequently, trigger Zn dendrite formation and proliferation (as illustrated in Fig. 1a). Moreover, Zn metal anodes experience side reactions during cycling, e.g., self-corrosion and hydrogen evolution reaction (HER), leading to the deterioration of Coulombic efficiency (CE) and the passivation of Zn anode surface. [7] Therefore, regulating uniform Zn²⁺ ion distribution and improving the thermodynamic stability of Zn metal in aqueous electrolyte are the fundamental solutions to realize uniform and stable Zn deposition.

Various strategies have been addressed to tackle the inherent shortcoming of Zn metal anodes. Focusing on the electrolyte modification, various functional additives such as polyacrylamide, [8] acetonitrile,

* Corresponding author.

E-mail address: licc@gdut.edu.cn (C.C. Li).

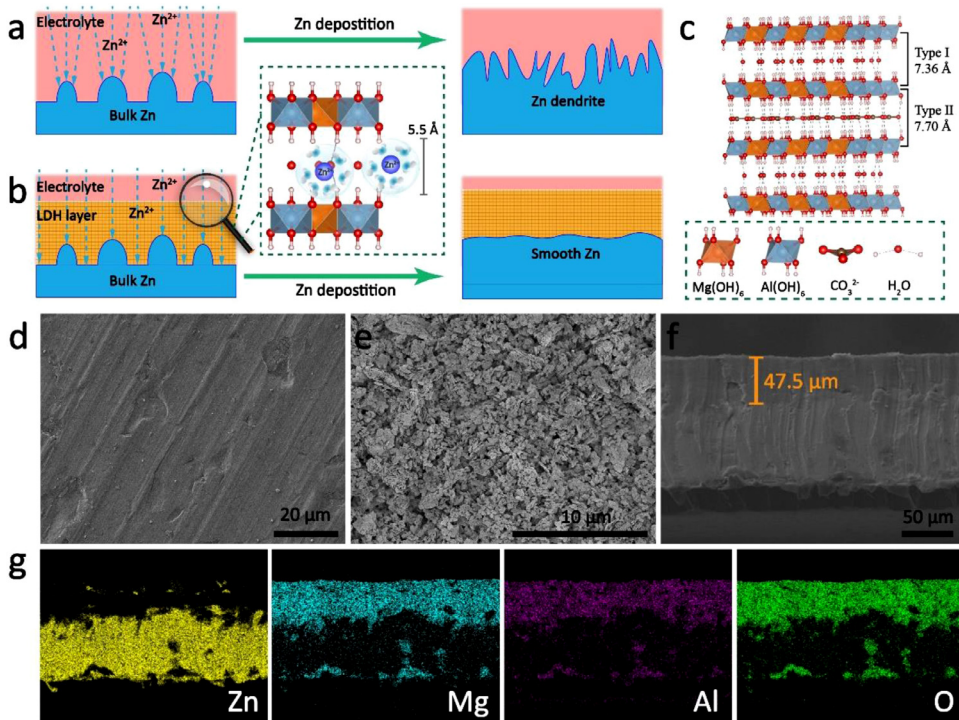


Fig. 1. Schematic diagrams illustrating the Zn deposition process (a) on the bare Zn and (b) on the Zn@LDH electrode. (c) The crystal structure of Mg-Al LDH and two types of layer structures in Mg-Al LDH. Surface SEM images of (d) the bare Zn and (e) Zn@LDH electrodes. (f) Cross-sectional SEM image and (g) corresponding elemental mapping of the Zn@LDH electrode.

[9] diethyl ether, [10] ethylene glycol, [11] polyethylene oxide [12] and tetrabutylammonium sulfate [13] have been adopted to suppress the dendrite growth by their electrostatic shielding interaction on Zn anode surfaces. Additionally, designing salt-concentrated electrolytes helps to eliminate H_2O from the $[\text{Zn}(\text{H}_2\text{O})_6]^{2+}$ solvation shell, which is verified to be effective for reducing HER and restraining the formation of Zn dendrites. However, the high cost of these Zn salts and relatively large voltage polarization resulting from their high viscosity may be underlying obstacles for the practical application of these electrolytes. On the other hand, a more simple and direct strategy is to fabricate inorganic, [14–19] organic, [20, 21] or inorganic/organic hybrid [3, 22–24] interfacial layers to stabilize the deposition interface. For instance, Cui et al. innovatively designed a $\text{Zn}(\text{TfO})_2$ /polyamide hybrid interphase to regulate the Zn deposition behavior and restrain electrolyte corrosion simultaneously. [23] Niu et al. assembled a uniform MXene layer to lower the Zn nucleation energy barrier and manipulate the surface electric field. [15] Despite great progresses have been made, current performance of Zn metal anodes is still unsatisfactory. In addition, the designed protective layers could inevitably cause increased internal impedance/polarization arising from its barrier effect on Zn^{2+} ion diffusion that occurs between the electrode and electrolyte. Therefore, there is still extensive advancement space for designing smart protective layers with fast Zn^{2+} transfer kinetics and the function of regulating Zn-ion flux to improve the electrochemical performance of Zn metal anodes.

It is well known that constructing the solid electrolyte interface (SEI) film as a functional protective layer on anodes to avoid the exfoliation of graphite during Li^+ insertion is one of the most important technological breakthroughs in the commercialization of LIBs. [25] Generally, an ideal SEI should meet the following requirements: (1) electron transference number $t_e = 0$; (2) high ion conductivity; (3) good mechanical strength and high stability in electrolytes. [26] Inspired by these, we propose the magnesium-aluminum layered double hydroxide (Mg-Al LDH) coating layer as a multifunctional artificial SEI for Zn metal anodes, which is in keeping with the above three criteria perfectly. As depicted in Fig. 1b, the layer structure with appropriate interlayer distance in Mg-Al LDH serves as ion channels for facile transport of Zn^{2+} ions. Abundant ion channels in Mg-Al LDH can effectively redistribute Zn-ion flux near the

interphase at a fundamental level, just like the spillway of a dam to dredge the flood, leading to an ultra-stable Zn plating/stripping behavior underneath the artificial SEI. Moreover, the highly stable and insulating LDH film can also substantially prevent electron tunneling and eliminate side reactions between Zn anode and electrolyte. Combining the advantages of excellent mechanical property, good chemical stability, and high ionic conductivity, the Mg-Al LDH artificial SEI allows high CE of 99.2% over 2000 cycles and ultralong cycle life (> 1400 h) with small voltage polarization (~ 31.6 mV at 0.5 mA cm^{-2}).

2. Result and discussions

Layered double hydroxides (LDHs) are a huge family of ionic lamellar compounds, which consist of positively charged brucite-like layers with an interlayer space containing solvation molecules and charge compensating anions. [27] Commercial Mg-Al LDH was used in this work, whose XRD patterns (Figure S1) show characteristic peaks of (003), (006), (012), (015), (018), (110) and (113) planes, in agreement with rhombohedral $(\text{Mg}_{0.667}\text{Al}_{0.333})(\text{OH})_2(\text{CO}_3)_{0.167}(\text{H}_2\text{O})_{0.5}$ (JCPDS No. 089-0460). As shown in Figure S2, Mg, Al, C and O elements are homogeneously distributed in Mg-Al LDH nanosheets. As shown in Fig. 1c, the Mg^{2+} and Al^{3+} cations are located at the center of the octahedron, and hydroxide anions occupy the vertexes which were connected to form a 2D infinite layer structure. Mg-Al LDH contains two different layer structures, in which the interlayer distance of the type I layer structure (7.70 Å) is slightly larger than that of the type II layer structure (7.36 Å) owing to the presence of interlayer CO_3^{2-} anions. Obviously, both interlayer regions are large enough to accommodate hydrated Zn^{2+} ions with a diameter of ~ 5.5 Å, which makes Mg-Al LDH a suitable host for facile Zn^{2+} transport potentially. SEM images were further obtained on the bare Zn and Zn@LDH electrodes to analyze the surface morphology (Fig. 1d–e). The surface of bare Zn is full of scratches and small pits formed during the manufacturing process (Fig. 1d). The rough surface of Zn foil will cause the concentration of Zn^{2+} ions near pits and crevices, and immensely disturb the distribution of Zn^{2+} ion flux at the electrode/electrolyte interface, consequently aggravating the growth of Zn dendrites. On the other hand, the Mg-Al LDH nanosheets ranging from 200 ~ 400 nm in size form a uniform coating on the Zn substrate

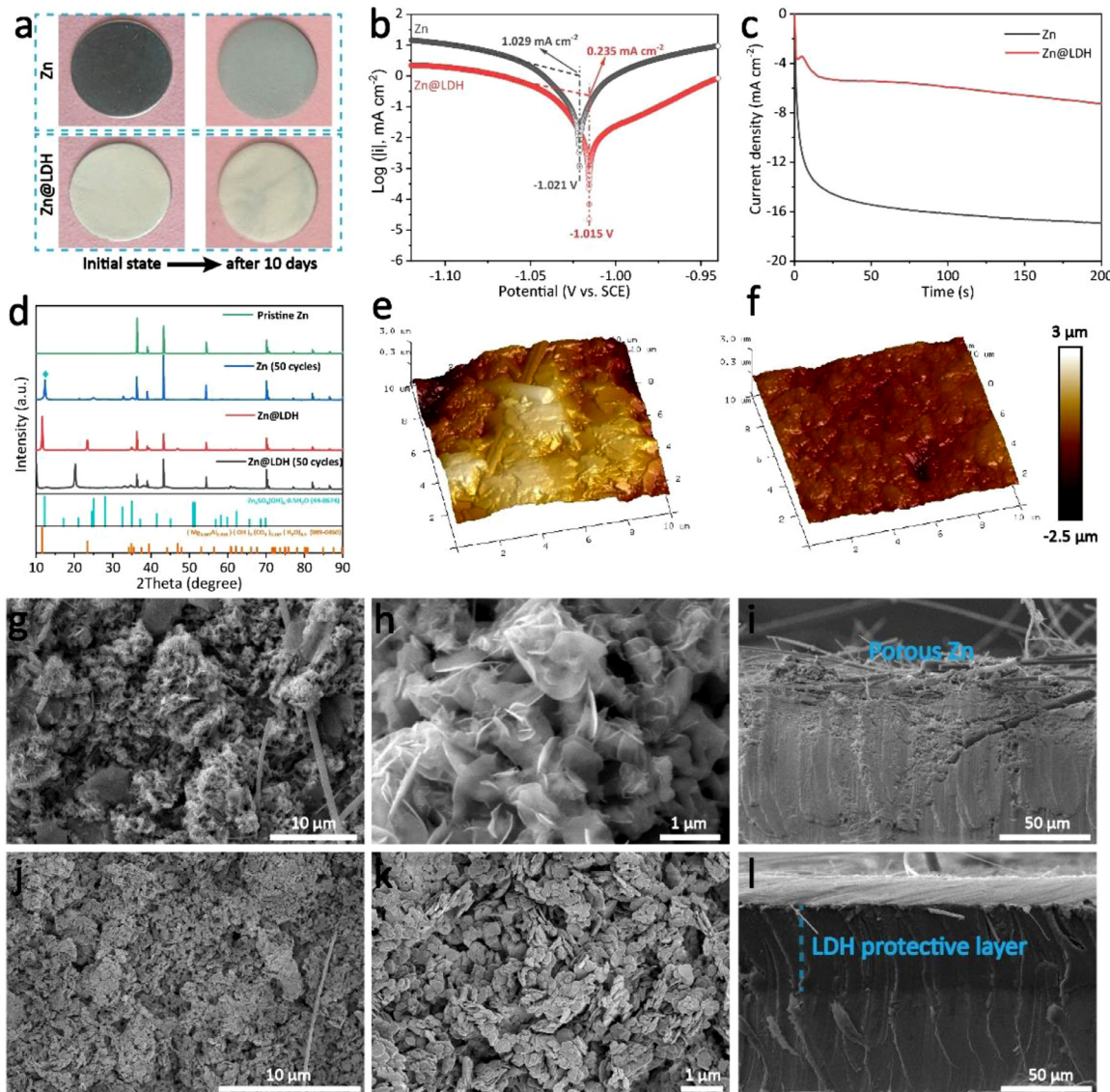


Fig. 2. (a) Photographs of corrosion morphology for the bare Zn and Zn@LDH electrodes after immersion in 2 M ZnSO₄ aqueous solution for 10 days. (b) Potentiodynamic polarization curves and (c) chronoamperograms (CAs) of the bare Zn and Zn@LDH electrodes in 2 M ZnSO₄ aqueous solution. (d) XRD patterns of the bare Zn and Zn@LDH electrodes after 50 cycles. AFM images of (e) the bare Zn and (f) Zn@LDH electrodes after 50 cycles. (g–h) The surface and (i) cross-sectional SEM images of the bare Zn after 50 cycles. (j–k) The surface and (l) cross-sectional SEM images of the Zn@LDH electrode after 50 cycles.

(Fig. 1e). The ultrathin nanosheet micromorphology of Mg-Al LDH is expected to provide reduced diffusion paths for ions, and endow rapid Zn²⁺ ion transport within the Mg-Al LDH interlayer spaces. The thickness of Mg-Al LDH layer is measured to be ~ 47.5 μm in the SEM image of Zn@LDH electrode on cross section view (Fig. 1f). Moreover, the hierarchical structure of Zn@LDH electrode can be more clearly distinguished in the elemental mapping images of Zn, Mg, Al, and O (Fig. 1g).

Mg-Al LDH films have been widely studied as effective inhibitors to improve the anti-corrosion abilities of Mg and Al alloys. [28–30] Therefore, it is reasonable to predict that the Mg-Al LDH film coating on Zn metal anodes may enhance its stability in electrolytes. To verify this hypothesis, both the bare Zn and Zn@LDH electrodes were immersed in the aqueous electrolyte containing 2.0 M ZnSO₄. The bare Zn tarnished after 10 days and an off-white by-products film was visible on the surface (Fig. 2a). In comparison, the Zn@LDH electrode surface remained basically unchanged after 10 days and no cracks nor protuberances were observed, revealing the excellent mechanical robustness and chemical stability of the Mg-Al LDH film. The polarization curves of the bare Zn and Zn@LDH electrodes in 2 M ZnSO₄ aqueous electrolyte were also ob-

tained to determine the corrosion protection ability of the Mg-Al LDH layer (Fig. 2b). Typically, a more positive corrosion potential (E_{corr}) or a smaller corrosion current density (i_{corr}) indicates a reduced corrosion reaction rate and a better corrosion resistance. The E_{corr} of Zn@LDH electrode (-1.015 V vs. SCE) is higher than that of bare Zn (-1.021 V vs. SCE). Moreover, the i_{corr} of Zn@LDH electrode (0.235 mA cm⁻²) is significantly lowered by almost 5 times compared with that of bare Zn (1.029 mA cm⁻²). The comparison clearly indicates that the anodic dissolution of Zn metal and cathodic HER in aqueous electrolyte is efficiently inhibited by the introduction of Mg-Al LDH protective layer. Furthermore, the chronoamperogram (CA) tests of both electrodes were also conducted to get deeper insights into the Zn deposition behavior (Fig. 2c). Under the constant overpotential of -0.15 V, the drastic change and ever-increasing time-current profile of bare Zn during the whole duration of 200 s suggests the rampant planar diffusion and rough deposition process. [31–34] For the Zn@LDH electrode, the incipient nucleation and two-dimensional diffusion behavior (corresponding to the similar slope portion of the time-current profile) exist within 20 s, and then the current density begins to increase extremely slowly in the lat-

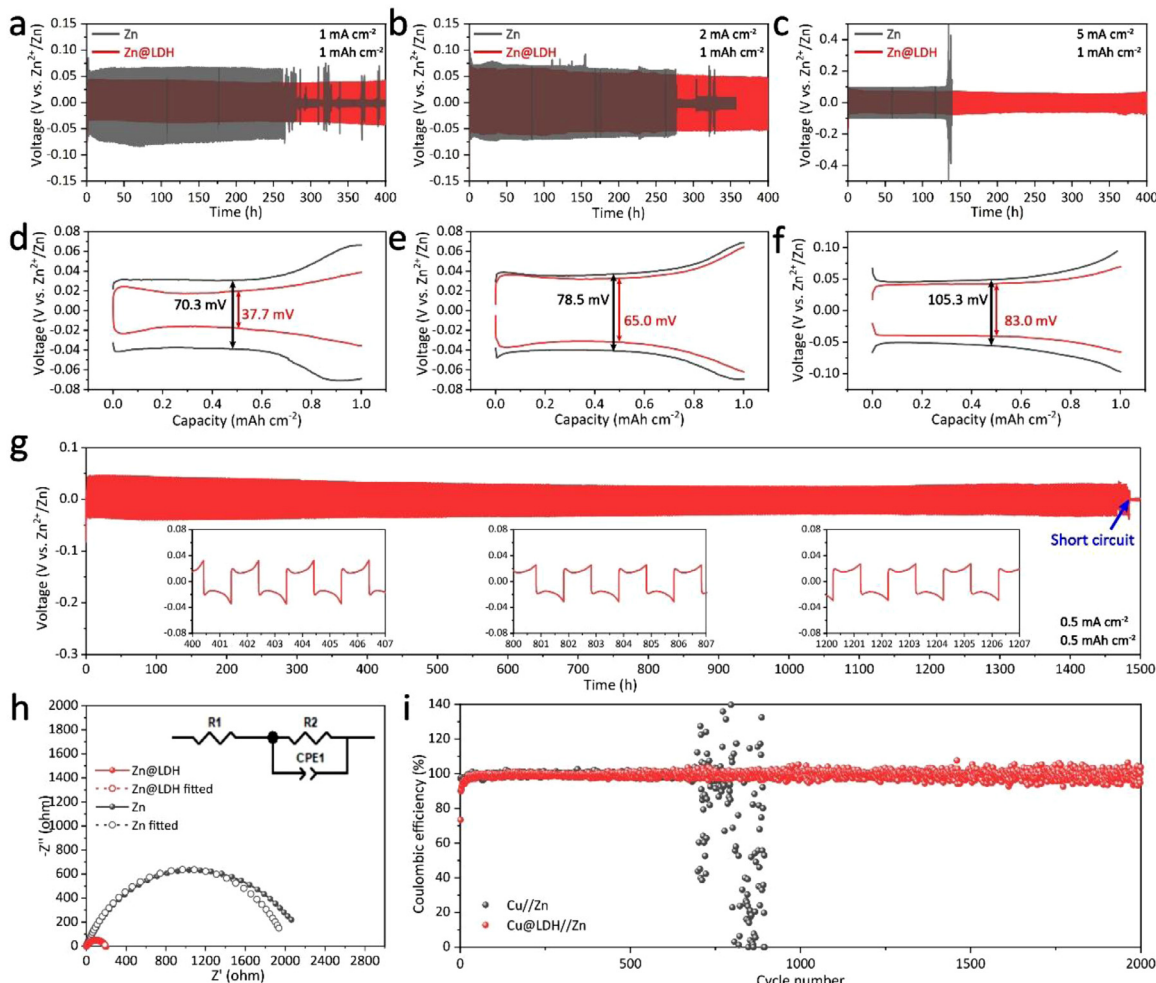
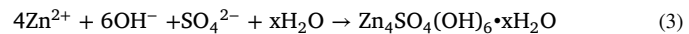


Fig. 3. Current-voltage profiles of the Zn//Zn and Zn@LDH//Zn@LDH symmetrical cells for 1 mAh cm⁻² at (a) 1 mA cm⁻², (b) 2 mA cm⁻² and (c) 5 mA cm⁻². The 100th cycle voltage profiles of the Zn//Zn and Zn@LDH//Zn@LDH symmetrical cells for 1 mAh cm⁻² at (d) 1 mA cm⁻², (e) 2 mA cm⁻² and (f) 5 mA cm⁻². (g) Long-term current-voltage profiles of the Zn@LDH//Zn@LDH symmetrical cells for 0.5 mAh cm⁻² at 0.5 mA cm⁻². (h) EIS of the Zn//Zn and Zn@LDH//Zn@LDH symmetrical cells. (i) CE of Zn plating/stripping on the bare Cu and Cu@LDH electrodes at 10 mA cm⁻², 1 mAh cm⁻².

ter part of the time-current profile (20–200 s) through 3D diffusion processes, which is indicative of compact zinc deposition. [19, 23, 35, 36]

The bending test of the Zn@LDH electrode after 50 cycles show that no powder flakes off the Zn substrate, and no noticeable cracks are observed (Figure S3), revealing the excellent mechanical strength and good adhesion between the Mg-Al LDH coating layer and Zn substrate. To find out whether the enhanced corrosion resistance and compact Zn deposition mechanism of the Zn@LDH electrode will contribute to the improved plating/stripping reversibility, both the bare Zn and Zn@LDH electrodes after 50 cycles were disassembled from symmetrical cells and investigated by XRD, AFM, and SEM characterizations (Fig. 2d-i). Compared with the bare Zn before cycling, a strong peak located at ~12.3° was observed in the XRD patterns of bare Zn after 50 cycles, corresponding to Zn₄SO₄(OH)₆•0.5H₂O by-products. It is generally accepted that the HER may occur during cycling due to a high desolvation energy barrier for the plating/stripping of solvated Zn²⁺ at the electrode/electrolyte interface. The HER generates OH⁻ locally and which will react with Zn²⁺ to produce an irreversible phase of Zn₄SO₄(OH)₆•xH₂O. The detailed reaction mechanism can be described by the following processes: [37]



On the contrary, the characteristic peak of Zn₄SO₄(OH)₆•0.5H₂O by-products is absent in XRD patterns of the Zn@LDH electrode after 50 cycles. It is worth mentioning that the (003) and (006) planes of Mg-Al LDH shift to lower degrees of 10.1° and 20.2°, respectively, suggesting that the interlayer distance of Mg-Al LDH has been broadened after cycling. This phenomenon may be associated with the ion-exchange between CO₃²⁻ in the interlamellar space and SO₄²⁻ in the electrolyte, which has been confirmed in previous reports about LDHs. [38] The expanded interlayer space should be beneficial to the fast Zn²⁺ diffusion by virtue of the decreased electrostatic repulsive force between the LDH host and intercalated Zn²⁺ ions. Furthermore, atomic force microscopy (AFM) was conducted to examine the surface topography of the bare Zn and Zn@LDH electrode after cycling (Fig. 2e-f). The uneven surface with pores and protrusions can be seen in the AFM image for the bare Zn after 50 cycles. While the surface of Zn@LDH electrode is very smooth and uniform (Fig. 2f), demonstrating that the LDH layer is consistently coated on the Zn substrate homogeneously during prolonged cycling. This outstanding uniformity is favorable for homogenizing Zn²⁺ ion flux and making Zn plating more smooth. SEM images were further obtained to investigate the detailed morphologies (Fig. 2g-l). The surface SEM images of the bare Zn electrode after 50 cycles show vertical leaf-like Zn dendrites (Fig. 2g-h). What's worse, porous and uneven Zn deposition

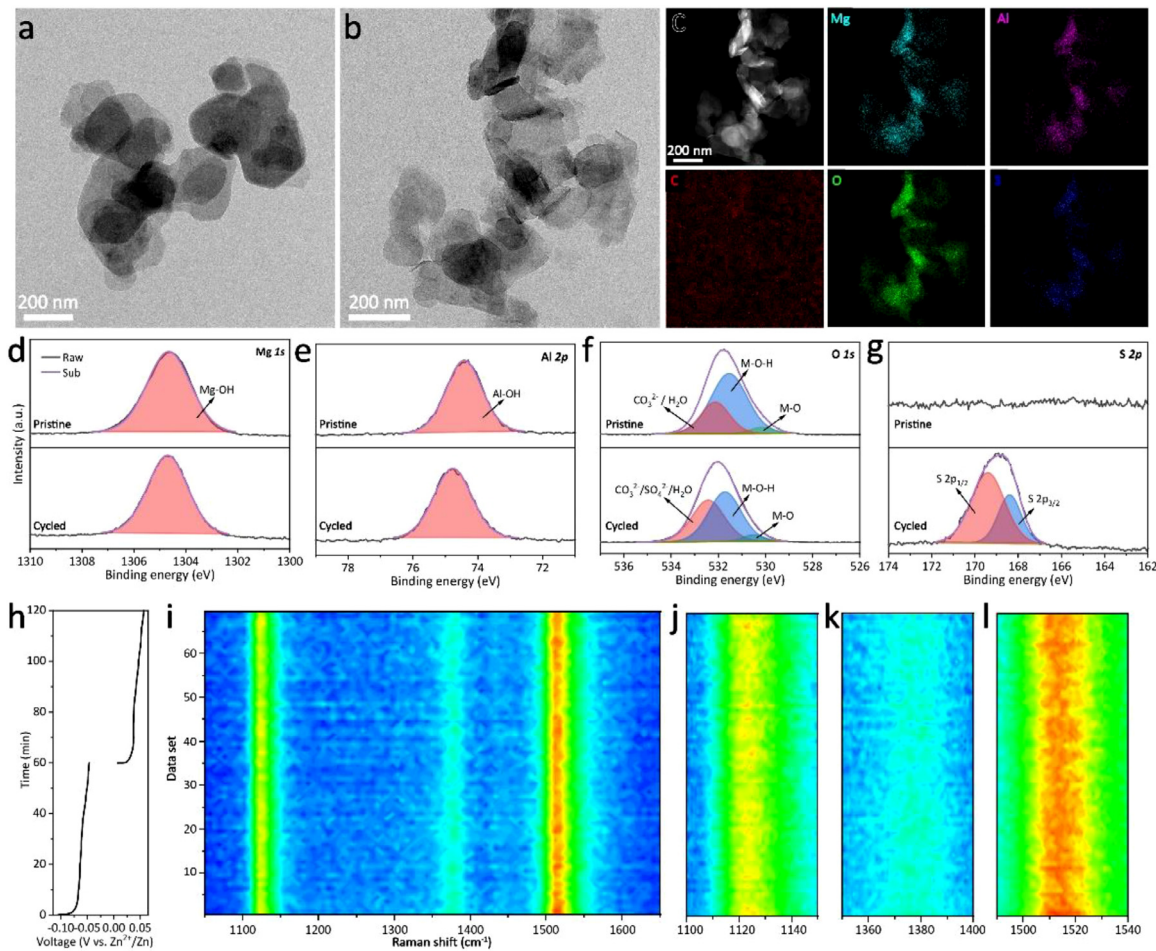


Fig. 4. TEM images of Mg-Al LDH (a) before cycling and (b) after 50 cycles. (c) HAADF image and corresponding elemental mapping of Mg-Al LDH after 50 cycles. High-resolution XPS spectra of pristine and cycled Mg-Al LDH for (d) Mg 1s, (e) Al 2p, (f) O 1s, and (g) S 2p. (h-l) Zn plating/stripping curve obtained for the Zn@LDH//Zn@LDH symmetrical cell and its real-time Raman contour map.

with severe agglomeration can be detected on the cross-sectional SEM images (Fig. 2i), which will aggravate the formation of dendritic Zn. While the surface morphology of the Zn@LDH electrode after cycling is similar to the original one without distinct change, and no vertical Zn dendrites or protuberances are observed (Fig. 2j-k). Furthermore, the cross-sectional SEM image shows dense and smooth Zn deposition (Fig. 2l), indicating that regulated Zn plating can be achieved underneath the Mg-Al LDH protective layer. We also tried to peel off the Mg-Al LDH layer of the Zn@LDH electrode after 50 cycles by using the doctor blade and ultrasonic treatment. As shown in Figure S4, the deposited Zn underneath the coating layer shows dense plate-like morphology ranging from 10 to 30 μm with the thickness of 1–2 μm . And negligible nanosheet dendrite or corrosion was detected on the surface of Zn substrate after 50 cycles.

The Mg-Al LDH protective layer serves as an artificial SEI film to provide Zn²⁺ diffusion channels and prevent the direct contact between electrolyte and Zn anode simultaneously, which is expected to afford superior electrochemical performance. Thus, the Zn//Zn and Zn@LDH//Zn@LDH symmetrical cells were assembled and evaluated (Fig. 3). When subjected to a fixed plating/stripping capacity of 1 mAh cm⁻² at the current density of 1 mA cm⁻² (Fig. 3a, d), the Zn@LDH//Zn@LDH symmetrical cell maintains superior stability and smaller voltage hysteresis (\sim 37.7 mV) over 400 h compared with that of the Zn//Zn symmetrical cell (\sim 70.3 mV). While the current-voltage profiles of the Zn//Zn symmetrical cell fluctuated dramatically and failed after about 265 h. The more obvious comparison is also observed for the

time-voltages profiles of both cells at the higher current densities of 2 mA cm⁻² (Fig. 3b) and 5 mA cm⁻² (Fig. 3c), demonstrating the enhanced cycling stability and rate capability of the Zn@LDH//Zn@LDH symmetrical cell. As depicted in Fig. 3e and f, the plating/stripping polarizations of the Zn@LDH//Zn@LDH symmetrical cells at higher current densities (65.0 and 83.0 mV at 2 and 5 mA cm⁻², respectively) are also much smaller than those of the Zn//Zn symmetrical cell (78.5 and 105.3 mV at 2 and 5 mA cm⁻², respectively), implying the fast Zn²⁺ transport kinetics in the Mg-Al LDH film. Importantly, the Zn@LDH//Zn@LDH symmetrical cell delivers stable Zn plating/stripping voltage profiles of impressively long cyclability exceeding 1400 h with low voltage polarization of 31.6 mV under 0.5 mA cm⁻² for 0.5 mAh cm⁻² (Fig. 3g). The cycle life of Zn@LDH electrode is comparable to most modified Zn metal anodes reported in literatures (Table S1). We also fabricated a Mg-Al LDH coating layer on the surface of Zn foil with the smaller thickness of \sim 22.3 μm (Figure S5) and evaluated its electrochemical performance. The current-voltage profiles of the as-prepared Zn@LDH electrode maintains stably without dramatical fluctuation at the current densities of 1 and 5 mA cm⁻² (Figure S6). Moreover, no Zn dendrites or cracks were found on the surface of the Zn@LDH electrode after 50 cycles (Figure S7), revealing that the MgAlO coating layer with a smaller thickness of \sim 22.3 μm can also prevent the growth of Zn dendrites effectively.

The striking difference in voltage hysteresis of both symmetrical cells may be related to the interfacial stability. As shown in Fig. 3h, the interfacial impedance of the Zn@LDH//Zn@LDH symmetrical cell (195.2 Ω) is significantly reduced compared with the Zn//Zn symmetrical cell

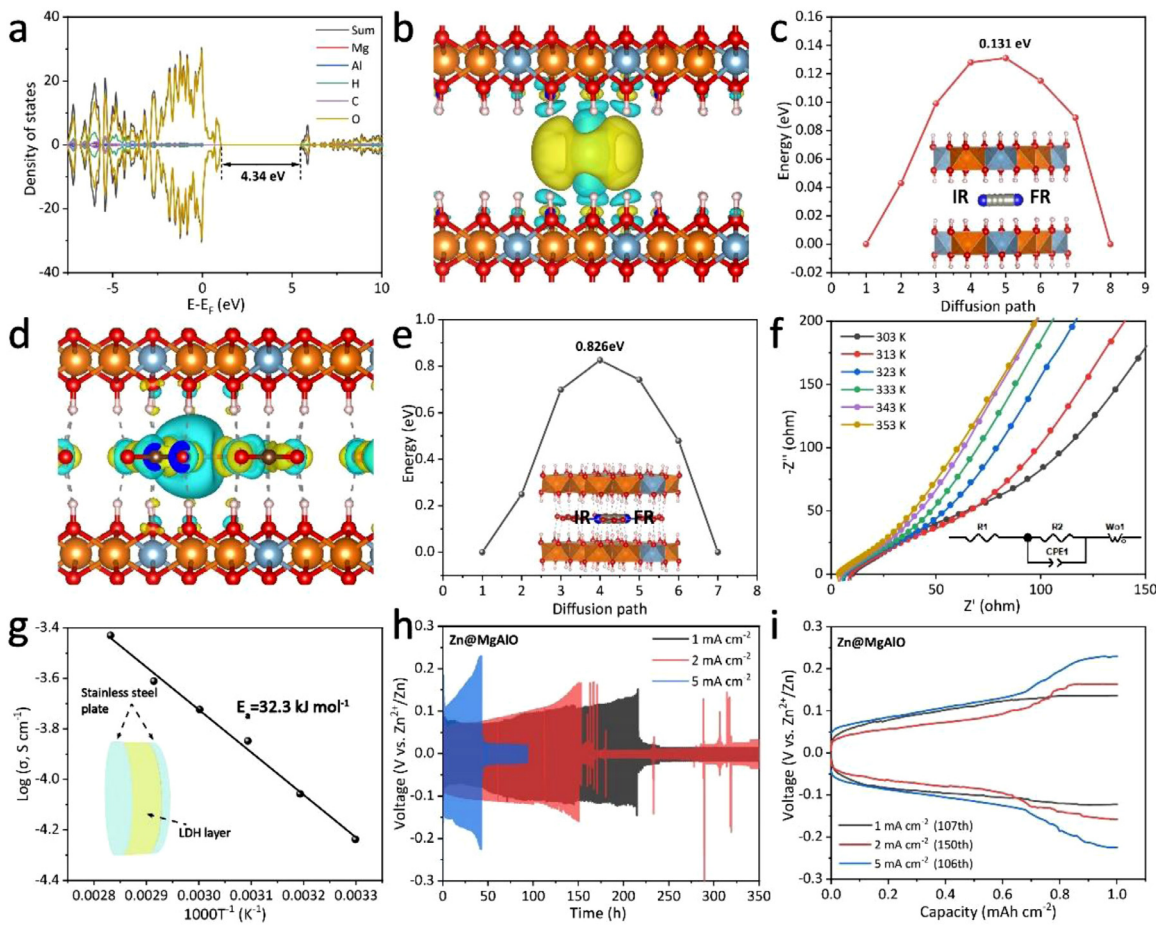


Fig. 5. (a) The partial density of states (PDOS) of Mg-Al LDH. (b) The charge density distribution plots and (c) diffusion energy barriers of Zn^{2+} ion within the Type I layer structure of Mg-Al LDH (inset is the diffusion path). (d) The charge density distribution plots and (e) diffusion energy barriers of Zn^{2+} ion within the Type II layer structure of Mg-Al LDH (inset is the diffusion path). (f) Nyquist plots of the Mg-Al LDH film measured between 303 and 353 K. (g) Arrhenius plots of the ion conductivity for the Mg-Al LDH film (inset is the schematic of the measurement geometry). (h) The time-voltage profiles of Zn@MgAlO symmetrical cells at various current densities. (i) Typical voltage profiles of Zn@MgAlO symmetrical cells at different current densities before the internal short-circuit.

(2021.0 Ω), demonstrating the stabilizing effect of the Mg-Al LDH coating. Besides, the CE is also a crucial indicator to evaluate the reversibility and durability of Zn metal anodes. Therefore, an Mg-Al LDH coating layer was fabricated on the surface of Cu foil to obtain the Cu@LDH electrode. As shown in Fig. 3i, the CE of Cu//Zn half cell fluctuated violently after only 740 cycles at 10 mA cm^{-2} , 1 mAh cm^{-2} due to the continuous accumulation of dead Zn. While a high average CE of 99.2% is maintained for the Cu@LDH//Zn half cell over 2000 cycles, illustrating the effectively inhibited side reactions by the Mg-Al LDH coating.

Building an ideal artificial SEI layer for Zn metal anodes should follow similar principles that have been extensively studied in LIB anodes. [39, 40] Accordingly, the structural stability of Mg-Al LDH during cycling is an accepted prerequisite, which is confirmed by TEM and XPS characterization of pristine and cycled Mg-Al LDH (Fig. 4a-g). TEM image of Mg-Al LDH after 50 cycles at 1 mA cm^{-2} , 1 mAh cm^{-2} (Fig. 4b) shows that LDH nanosheets are well retained without any morphological change compared with the original one (Fig. 4a). In addition, Mg, Al, O and S elements are also homogeneously distributed in the cycled Mg-Al LDH, and the presence of S element further corroborates ion-exchange between CO_3^{2-} and SO_4^{2-} . The distribution of C element is hard to be distinguished due to the disturbance of carbon film. As shown in Fig. 4d and e, the Mg 1s and Al 2p peaks of the pristine Mg-Al LDH are located at 1304.7 eV and 74.5 eV, corresponding to the bonding energies of Mg-OH and Al-OH, respectively. These two peaks are also observed in the cycled Mg-Al LDH without obvious shift and shape change, indicating the ro-

bust host structure made of $Mg(OH)_6$ and $Al(OH)_6$ octahedron. Both the O 1s XPS spectra at different states can be deconvoluted into three peaks, which can be assigned to M-O bond (~530.1 eV), M-OH (~531.5 eV) and $CO_3^{2-}(SO_4^{2-})/H_2O$ (~532.2 eV), respectively (Fig. 4f). Moreover, the relative peak area ratio of the $CO_3^{2-}(SO_4^{2-})/H_2O$ bond slightly increased from 28.3% to 43.4% after cycling, contributing to the ion-exchange process and the co-intercalated water. It is worth noting that the S signal of $S 2p_{1/2}$ (~169.4 eV) and $S 2p_{3/2}$ (~168.4 eV) is detected in the S 2p XPS spectra of Mg-Al LDH after 50 cycles (Fig. 4g), further confirming the ion-exchange effect. In situ Raman observation of the electrochemical interface during Zn plating/stripping was also conducted by using a home-made Raman electrochemical cell (Figure S8). The pristine Zn@LDH electrode exhibits three broad peaks at 1123, 1376, and 1514 cm^{-1} in the range of $1050 \sim 1650 \text{ cm}^{-1}$, matching well with the characteristic vibration modes of Mg-Al layered double hydroxide reported by previous literature. [28] The spectrum intensity of these peaks almost remains unchanged (Fig. 4i), and no Raman shift is observed (Fig. 4j-l), revealing the superb electrochemical stability of the Mg-Al LDH film during Zn plating/stripping. This evidence validates that Zn^{2+} transport through the interlayer spaces of Mg-Al LDH does not damage its crystalline structure. On basis of these results, it can be concluded that the Mg-Al LDH artificial SEI film can well preserve the structural integrity and chemical stability, and effectively tolerate the huge volume change during repeated Zn deposition/stripping.

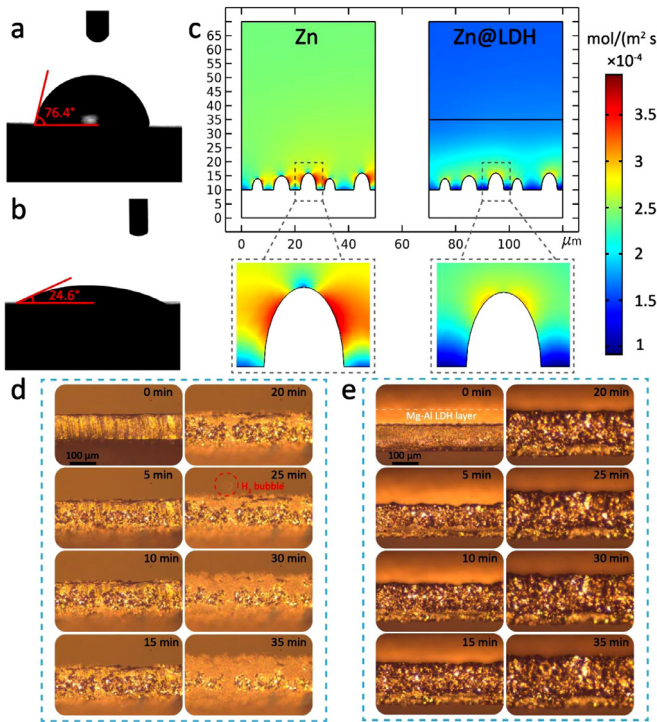


Fig. 6. Contact angles of electrolyte (a) on the bare Zn and (b) on the Zn@LDH electrode. (c) Simulation results of the Zn-ion flux distribution on the surface of bare Zn and Zn@LDH electrode. In situ optical microscope observation of Zn deposition at 10 mA cm^{-2} (d) on the bare Zn and (e) on the Zn@LDH electrode.

Besides the excellent chemical and mechanical stability, the Mg-Al LDH artificial SEI film is also expected to ensure facile Zn-ion transport at the interface through its interlayer ion channels. DFT calculations and corresponding experiments were conducted to confirm this assumption (Fig. 5). As shown in Fig. 5a, the bandgap of Mg-Al LDH is calculated to be as high as 4.34 eV, which can serve as a highly electron-insulating shielding layer to avoid electron tunneling from electrode to electrolyte. In order to make clear the effect of the intercalated Zn^{2+} ion on the electronic structure of Mg-Al LDH, the charge density distributions were obtained (Fig. 5b and d), in which yellow and blue regions represent charge accumulation and charge loss, respectively. [41] It is obvious that the charge density differences of Mg(OH)_6 and Al(OH)_6 octahedra change little after the intercalation of Zn^{2+} ion into both types of interlayer spaces, implying the outstanding stability of the crystal skeleton. Moreover, the low interaction energies between Zn^{2+} ions and the layer framework are beneficial to the fast ion diffusion. It should be noticed that a strong electronic interaction is observed between the inserted Zn^{2+} cation and CO_3^{2-} anions in Type II layer structure due to the electrostatic interaction (Fig. 5d). Strikingly, the Zn^{2+} diffusion energy barrier within the Type I layer structure of Mg-Al LDH is only 0.131 eV (Fig. 5c), which is significantly smaller than that of most ZIB electrode materials with intercalation mechanism such as $\text{V}_2\text{O}_5 \cdot \text{H}_2\text{O}$ (0.66 eV), [42] V_6O_{13} (0.87 eV), [43] VO_2 (0.24–0.71 eV), [44] $\text{VO}_2(\text{B})$ (0.586 eV), [45] MnO_2 (0.32 eV), [46] $\text{Na}_{0.14}\text{TiS}_2$ (0.55 eV), [47] $\text{KV}_2\text{O}_4\text{PO}_4 \cdot 3.2\text{H}_2\text{O}$ (0.66 eV), [48] VSe_2 (0.91 eV), [49] $\text{K}_2\text{V}_8\text{O}_{21-x}$ (0.63 eV), [50]. The Zn^{2+} diffusion energy barrier within the Type II layer structure is relatively higher (0.826 eV) owing to the existence of CO_3^{2-} anions in interlayer spaces (Fig. 5e), which is consistent with the charge density distribution analysis.

DFT calculation results reveal that Mg-Al LDH can provide favorable ion channels for fast Zn^{2+} migration, which is further validated by the measurement of temperature-dependent ion conductivities (Fig. 5f–g). The Mg-Al LDH film (thickness of $\sim 110 \mu\text{m}$) with 2 drops of elec-

trolyte added was sandwiched by two stainless steel plates (inset in Fig. 5g), and used for the measurement of electrochemical impedance spectroscopy (EIS). Nyquist plots of the Mg-Al LDH film obtained at different temperatures can be fitted by using the equivalent circuit model (inset in Fig. 5f), in which R_1 is the electrolyte resistance and R_2 represent the charge-transfer resistance. The Mg-Al LDH film achieves a high ionic conductivity (σ) of $5.24 \times 10^{-5} \text{ S cm}^{-1}$ at 30°C (Fig. 5g), which is even comparable to that of many solid lithium-ion electrolytes such as $\text{Li}_{0.34(1)}\text{La}_{0.51(1)}\text{TiO}_{2.94(2)}$ (LLTO, $2 \times 10^{-5} \text{ S cm}^{-1}$), [51] $\text{Li}_7\text{La}_3\text{Zr}_2\text{O}_{12}$ (LLZO, $2 \times 10^{-6} \text{ S cm}^{-1}$), [52] $\text{Li}_{4+x+\delta}-(\text{Ge}_{1-\delta'-x}\text{Ga}_x)\text{S}_4$ ($6.5 \times 10^{-5} \text{ S cm}^{-1}$), [53] and $\text{Li}_{2.88}\text{PO}_{3.73}\text{N}_{0.14}$ (LiPON, $3.3 \times 10^{-6} \text{ S cm}^{-1}$). [54] In addition, the dependence of ionic conductivities for the Mg-Al LDH film can be well fitted by using the Arrhenius formula: [55, 56]

$$\sigma = A \exp\left(-\frac{E_a}{RT}\right)$$

where A is the pre-exponential factor, E_a is the activation energy, T is the absolute temperature and R is the gas constant. Consequently, E_a of the Mg-Al LDH film is calculated to be only 32.3 kJ mol^{-1} . To validate the function of unobstructed ion channels in the artificial SEI, the Mg-Al LDH was calcinated at 500°C for 3 h to destroy the layer structure. As shown in Figure S9, the as-prepared product is the mixture of MgO and Al_2O_3 (denoted as MgAlO) with poor crystallinity, which was coated on the surface of Zn to obtain the Zn@MgAlO electrode. Owing to the insufficient ion pathway in the MgAlO film, the polarization of Zn@MgAlO electrode increases continuously during cycling, and resulting in battery failure after 214 h at 1 mA cm^{-2} with a plating/stripping capacity of 1 mAh cm^{-2} (Fig. 5h). The more apparent trend can be identified in the time-voltage profiles at higher current densities of 2 and 5 mA cm^{-2} . Before the occurrence of the internal short circuit, the voltage gaps of Zn@MgAlO symmetrical cells are approximately 209.8, 166.4, and 233.3 mV at 1, 2, and 5 mA cm^{-2} , respectively, which are even larger than that of Zn//Zn symmetrical cells (Fig. 5i). Due to the absence of layered structure in MgAlO, the ionic conductivity (σ) of the MgAlO film is only $5.24 \times 10^{-7} \text{ S cm}^{-1}$ at 30°C (Figure S10a). In addition, E_a of the MgAlO film is increased to 50.7 kJ mol^{-1} (Figure S10b). The distinct contrast of electrochemical performance between the Zn@LDH and Zn@MgAlO symmetrical cells firmly demonstrates the important role of fast ion channels in the protective layer.

To investigate the wettability of both electrodes, contact angle measurements were carried out using 2 M ZnSO_4 aqueous solution as the electrolyte. As shown in Fig. 6a and b, the contact angle of electrolyte on the Zn@LDH electrode (24.6°) is much smaller compared with bare Zn (76.4°). The improved affinity between the LDH coating layer and electrolyte guarantees the homogenous concentration gradient of Zn^{2+} ions at the electrode/electrolyte interface. The distribution of Zn^{2+} ion flux on the bare Zn and Zn@LDH electrode was further monitored by using the COMSOL Multiphysics software (Fig. 6c). And several protrudes were constructed on the planner substrate to simulate the roughness surface of Zn foil. For the bare Zn, Zn^{2+} ions tend to accumulate near these protuberances, causing uneven ion distribution. These red regions with much enhanced Zn-ion flux will undoubtedly induce amplified Zn growth, which can be seen as “hot spots” for Zn dendrite formation. [57] By contrast, with an Mg-Al LDH coating layer on the surface, Zn-ion flux is effectively redistributed and homogenized, contributing to the uniform Zn plating. The Zn deposition behavior on both electrodes was further investigated by the in situ optical microscope observation at the current density of 10 mA cm^{-2} (Fig. 6d–e). Loose and isolated Zn dendrites were observed on the bare Zn after only 5 min of deposition, which forms serious mossy-like agglomeration after 35 min (Fig. 6d, Video S1). To make matters worse, H_2 bubbles were generated continuously, severely perturbing Zn plating. In striking contrast, the Zn@LDH electrode exhibited a dense and smooth deposition morphology, and the evolution of H_2 bubbles completely disappeared during the whole Zn plating process under the same condition (Fig. 6e, Video S2). Because the optical microscope relies on the reflection of light by the object to ob-

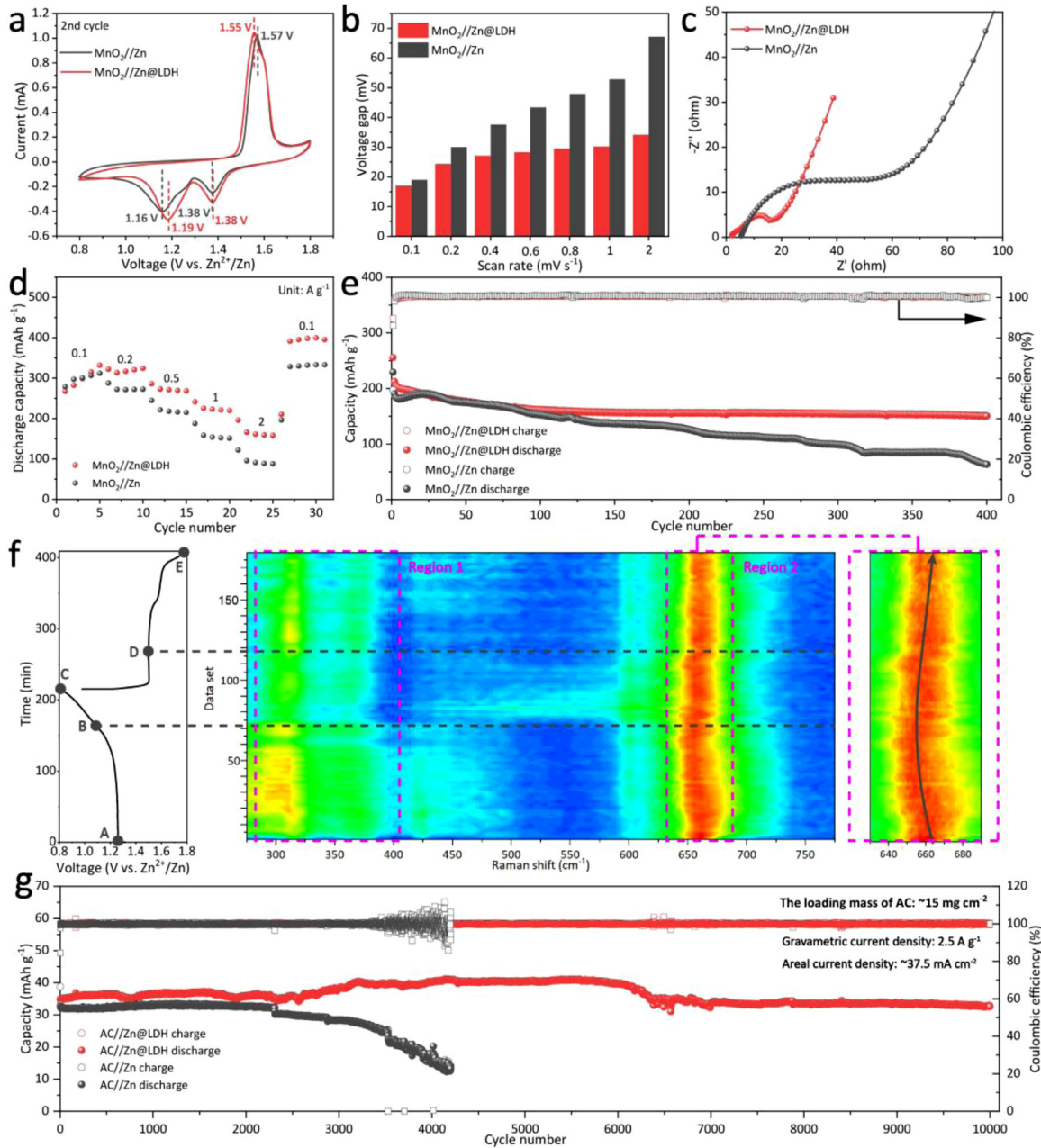


Fig. 7. (a) CV profiles of the MnO_2/Zn and $\text{MnO}_2/\text{Zn@LDH}$ cells between 0.8 and 1.8 V at 0.1 mV s⁻¹ during the 2nd cycle. (b) Voltage gaps of the MnO_2/Zn and $\text{MnO}_2/\text{Zn@LDH}$ cells at different scan rates. (c) EIS of the MnO_2/Zn and $\text{MnO}_2/\text{Zn@LDH}$ cells after 5 cycles. (d) Rate performance and (e) cycling stability of the MnO_2/Zn and $\text{MnO}_2/\text{Zn@LDH}$ cells at the current density of 1 A g⁻¹. (f) The charge/discharge profiles and in situ Raman contour image of the $\beta\text{-MnO}_2$ electrode recorded during the initial cycle in the $\text{MnO}_2/\text{Zn@LDH}$ cell. (g) Cycling performance of the AC//Zn and AC//Zn@LDH ZICs at the current density of 2.5 A g⁻¹.

tain image, the pure white Mg-Al LDH coating layer is hard to be clearly observed in the optical microscope image due to its ultralow reflectivity. It should be noticed that the Mg-Al coating layer becomes more and more indistinct during the Zn deposition process, due to the continuous Zn deposition from the boundary between the Zn substrate and Mg-Al coating layer, which may disturb the observation of the coating layer.

To verify the feasibility of the Zn@LDH electrode, the bare Zn and Zn@LDH electrodes were paired with $\beta\text{-MnO}_2$ cathode to test the full-cell electrochemical performance. As shown in Fig. 7a, both the CV curves of the MnO_2/Zn and $\text{MnO}_2/\text{Zn@LDH}$ full cells at 0.1 mV s⁻¹ exhibit two reduction peaks and the overlapped oxidation peaks, which correspond to the intercalation/deintercalation of proton and Zn^{2+} ions. However, the voltage gap of the $\text{MnO}_2/\text{Zn@LDH}$ cell (1.38/1.55 V) is

smaller than that of the MnO_2/Zn cell (1.38/1.57 V). More distinct differences of voltage gap can be found in CV curves at higher scan rates (Fig. 7b, S11), revealing the diminished electrochemical polarization of the $\text{MnO}_2/\text{Zn@LDH}$ cell, especially at high rates. The electrochemical polarization is related to the charge-transfer resistance (R_{ct}), which is reflected by the semicircle in the high to medium frequency region in EIS. The R_{ct} of the $\text{MnO}_2/\text{Zn@LDH}$ cell is much lower than that of the MnO_2/Zn cell due to the stabilized interface by the functional Mg-Al LDH coating layer (Fig. 7c). Rate performance of both cells are displayed in Fig. 7d. The discharge capacity of the $\text{MnO}_2/\text{Zn@LDH}$ cell after 5 cycles activation at 1 A g⁻¹ is 331.9 mAh g⁻¹, which is close to that of the MnO_2/Zn cell (312.0 mAh g⁻¹). But the Zn@LDH anode affords full cells with better rate capability. With the stepwise increasing

current densities of 0.2, 0.5, 1, and 2 A g⁻¹, the average capacities of the MnO₂//Zn@LDH cell can reach 319.5, 273.5, 226.1, and 168.0 mAh g⁻¹, while those of the MnO₂//Zn cell are only 275.6, 218.9, 154.0, and 89.6 mAh g⁻¹.

Besides improved rate performance, the MnO₂//Zn@LDH cell also exhibits superior cycling stability benefiting from the suppression of Zn dendrite formation and HER during cycling. Consequently, a high reversible capacity of 150.6 mAh g⁻¹ with a high capacity retention of 75.3% can be retained after 400 cycles at 1 A g⁻¹ (Figure 7e). By comparison, the capacity of the MnO₂//Zn cell decays dramatically from 182.6 mAh g⁻¹ to 63.4 mAh g⁻¹, corresponding to a low capacity retention of 34.7%. In situ Raman spectroscopy was employed to investigated the structure evolution of β -MnO₂ cathode in the MnO₂//Zn@LDH cell during cycling (Fig. 7f). Two weak peaks located at 317 and 373 cm⁻¹ (region 1) are attributed to B_g and E_u vibrational active modes of MnO₂, respectively, which are concerned with tunnel ions. And the strong peak at 659 cm⁻¹ (region 2) is related to the A_{1g} vibration mode of MnO₆ octahedral double chains. [58–60] The strong peak in region 2 shows a redshift trend during the discharge process, and gradually recovers to its initial position during the charging process. Moreover, the intensity of these two peaks in region 1 remain unchanged during the flat voltage curve range of AB but decay significantly in the sloping voltage curve range of BC, indicating that the crystalline structure change induced by ions insertion during the final discharge process is relatively large. However, these peaks basically recover to their initial states after charging to 1.8 V, confirming the excellent stability of the MnO₂ host structure. These results provide strong evidence for the reversible ion intercalation/deintercalation processes MnO₂//Zn@LDH cell, which may be also associated with the fast Zn²⁺ plating/stripping kinetics on the Zn@LDH anode.

Owing to the intrinsic low electrochemical kinetics of MnO₂ cathode, Zn//MnO₂-based zinc-ion batteries may not meet the requirement for high power applications. Therefore, we also fabricated hybrid zinc-ion capacitors (ZICs) coupled with commercial active carbon (AC) cathodes. Benefiting from the excellent Zn²⁺ plating/stripping reversibility of Zn@LDH electrode at high rates, the loading mass of AC in cathodes can reach up to 15 mg cm⁻². When cycled between 0.2 and 2.0 V, the AC//Zn@LDH ZIC maintains 93.7% of its initial capacity (~34.8 mAh g⁻¹) corresponding to an average CE exceeding 99.9% after more than 10000 cycles at the high areal current density of 37.5 mA cm⁻² (Fig. 7g, S12). While the AC//Zn ZIC decays to 13.3 mAh g⁻¹ after only 4200 cycles, and the CEs are destabilized aggressively after 3500 cycles owing to the ever-increasing formation of dead Zn. As shown in Table S2, the electrochemical performance of the Zn@LDH//AC hybrid ZICs are prominent compared with other Zn-based aqueous supercapacitors in terms of loading mass, areal current densities and capacity retention.

3. Conclusions

In conclusion, an Mg-Al LDH-based artificial SEI was fabricated on the surface of Zn foil to inhibit the growth of Zn dendrites and prevent side reactions. The well-aligned layer structure in Mg-Al LDH exhibit the lowest diffusion energy barrier of only 0.131 eV, which can serve as rapid ion channels for redistributing Zn-ion flux at the interface. In addition, in situ Raman, ex situ XRD and ex situ XPS measurements of the Zn@LDH electrode proved the excellent stability of the artificial SEI, which can effectively inhibit H₂O-induced corrosion and HER during electrochemical cycling. The prominent advantages of Mg-Al LDH-based artificial SEI render an ultra-stable and dendrite-free Zn deposition behavior, verified by in-situ optical microscope observation, ex-situ SEM and COMSOL numerical simulation. Consequently, the Zn@LDH electrode exhibits high Coulombic efficiency of 99.2% over 2000 cycles and ultralong cycle life (> 1400 h) with low voltage polarization (~31.6 mV at 0.5 mA cm⁻²). Moreover, zinc-ion full cells and zinc-ion capacitors using the Zn@LDH electrode as anode display remarkable cycling stability and rate capability. The rational design of Mg-Al LDH-based artificial

SEI provides a fundamental and fresh insight into the development of highly stable and reversible Zn metal anodes toward next-generation aqueous electrochemical energy storage technologies.

Data availability

The data that has been used is confidential.

Declaration of Competing Interest

The authors declare that they have no known competing financial interests or personal relationships that could have appeared to influence the work reported in this paper.

CRediT authorship contribution statement

Yang Yang: Conceptualization, Methodology, Investigation, Writing - original draft. **Chaoyue Liu:** Software. **Zeheng Lv:** Investigation. **Hao Yang:** Investigation. **Xian Cheng:** Investigation. **Shengzhao Zhang:** Investigation. **Minghui Ye:** Validation. **Yufei Zhang:** Visualization. **Libao Chen:** Writing - review & editing. **Jinbao Zhao:** Supervision. **Cheng Chao Li:** Writing - review & editing.

Acknowledgments

This work was supported by Guangdong Basic and Applied Basic Research Foundation (No. 2019A1515111069, No. 2021A1515010177) and National Natural Science Foundation of China (No. 51771058, No. 51971066).

Supplementary materials

Supplementary material associated with this article can be found, in the online version, at doi:[10.1016/j.ensm.2021.06.002](https://doi.org/10.1016/j.ensm.2021.06.002).

References

- [1] A. Wang, S. Tang, D. Kong, S. Liu, K. Chiou, L. Zhi, J. Huang, Y.-Y. Xia, J. Luo, Bend-Tolerant Anodes for Lithium-Metal Batteries, *Adv. Mater.* 30 (2018) 1703891.
- [2] Y. Zhao, Y. Zhu, X. Zhang, Challenges and perspectives for manganese-based oxides for advanced aqueous zinc-ion batteries, *InfoMat* 2 (2020) 237–260.
- [3] H. Yang, Y. Qiao, Z. Chang, H. Deng, P. He, H. Zhou, A Metal-Organic Framework as a Multifunctional Ionic Sieve Membrane for Long-Life Aqueous Zinc-Iodide Batteries, *Adv. Mater.* 32 (2020) 2004240.
- [4] J. Huang, J. Zhou, S. Liang, Guest Pre-Intercalation Strategy to Boost the Electrochemical Performance of Aqueous Zinc-Ion Battery Cathodes, *Acta Phys. -Chim. Sin.* 37 (2021) 2005020.
- [5] W. Yang, X. Du, J. Zhao, Z. Chen, J. Li, J. Xie, Y. Zhang, Z. Cui, Q. Kong, Z. Zhao, C. Wang, Q. Zhang, G. Cui, Hydrated Eutectic Electrolytes with Ligand-Oriented Solvation Shells for Long-Cycling Zinc-Organic Batteries, *Joule* 4 (2020) 1557–1574.
- [6] C. Zhang, S. Liu, G. Li, C. Zhang, X. Liu, J. Luo, Incorporating Ionic Paths into 3D Conducting Scaffolds for High Volumetric and Areal Capacity, High Rate Lithium-Metal Anodes, *Adv. Mater.* 30 (2018) 1801328.
- [7] L.E. Blanc, D. Kundu, L.F. Nazar, Scientific Challenges for the Implementation of Zn-Ion Batteries, *Joule* 4 (2020) 771–799.
- [8] Q. Zhang, J. Luan, L. Fu, S. Wu, Y. Tang, X. Ji, H. Wang, The Three-Dimensional Dendrite-Free Zinc Anode on a Copper Mesh with a Zinc-Oriented Polyacrylamide Electrolyte Additive, *Angew. Chem. Int. Ed.* 58 (2019) 15841–15847.
- [9] J. Shi, K. Xia, L. Liu, C. Liu, Q. Zhang, L. Li, X. Zhou, J. Liang, Z. Tao, Ultrahigh coulombic efficiency and long-life aqueous Zn anodes enabled by electrolyte additive of acetonitrile, *Electrochim. Acta* 358 (2020) 136937.
- [10] W. Xu, K. Zhao, W. Huo, Y. Wang, G. Yao, X. Gu, H. Cheng, L. Mai, C. Hu, X. Wang, Diethyl ether as self-healing electrolyte additive enabled long-life rechargeable aqueous zinc ion batteries, *Nano Energy* 62 (2019) 275–281.
- [11] N. Wang, Y. Yang, X. Qiu, X.L. Dong, Y.G. Wang, Y.Y. Xia, Stabilized Rechargeable Aqueous Zinc Batteries Using Ethylene Glycol as Water Blocker, *Chemsuschem* 13 (2020) 5556–5564.
- [12] Y. Jin, K.S. Han, Y. Shao, M.L. Sushko, J. Xiao, H. Pan, J. Liu, Stabilizing Zinc Anode Reactions by Polyethylene Oxide Polymer in Mild Aqueous Electrolytes, *Adv. Funct. Mater.* 30 (2020) 2003932.
- [13] A. Bayaguid, X. Luo, Y. Fu, C. Zhu, Cationic Surfactant-Type Electrolyte Additive Enables Three-Dimensional Dendrite-Free Zinc Anode for Stable Zinc-Ion Batteries, *ACS Energy Lett* 5 (2020) 3012–3020.
- [14] D. Han, S. Wu, S. Zhang, Y. Deng, C. Cui, L. Zhang, Y. Long, H. Li, Y. Tao, Z. Weng, Q.H. Yang, F. Kang, A Corrosion-Resistant and Dendrite-Free Zinc Metal Anode in Aqueous Systems, *Small* 16 (2020) 2001736.

- [15] N. Zhang, S. Huang, Z. Yuan, J. Zhu, Z. Zhao, Z. Niu, Direct Self-Assembly of MXene on Zn Anodes for Dendrite-Free Aqueous Zinc-Ion Batteries, *Angew. Chem. Int. Ed.* 60 (2020) 2861–2865.
- [16] M. Liu, J. Cai, H. Ao, Z. Hou, Y. Zhu, Y. Qian, NaTi₂(PO₄)₃ Solid-State Electrolyte Protection Layer on Zn Metal Anode for Superior Long-Life Aqueous Zinc-Ion Batteries, *Adv. Funct. Mater.* 30 (2020) 2004885.
- [17] L.T. Kang, M.W. Cui, F.Y. Jiang, Y.F. Gao, H.J. Luo, J.J. Liu, W. Liang, C.Y. Zhi, Nanoporous CaCO₃ Coatings Enabled Uniform Zn Stripping/Plating for Long-Life Zinc Rechargeable Aqueous Batteries, *Adv. Energy Mater.* 8 (2018) 1801090.
- [18] X. Xie, S. Liang, J. Gao, S. Guo, J. Guo, C. Wang, G. Xu, X. Wu, G. Chen, J. Zhou, Manipulating the ion-transfer kinetics and interface stability for high-performance zinc metal anodes, *Energy Environ. Sci.* 13 (2020) 503–510.
- [19] C. Deng, X. Xie, J. Han, Y. Tang, J. Gao, C. Liu, X. Shi, J. Zhou, S. Liang, A Sieve-Functional and Uniform-Porous Kaolin Layer toward Stable Zinc Metal Anode, *Adv. Funct. Mater.* 30 (2020) 2000599.
- [20] J. Hao, X. Li, S. Zhang, F. Yang, X. Zeng, S. Zhang, G. Bo, C. Wang, Z. Guo, Designing Dendrite-Free Zinc Anodes for Advanced Aqueous Zinc Batteries, *Adv. Funct. Mater.* 30 (2020) 2001263.
- [21] Q. Yang, Y. Guo, B. Yan, C. Wang, Z. Liu, Z. Huang, Y. Wang, Y. Li, H. Li, L. Song, J. Fan, C. Zhi, Hydrogen-Substituted Graphdiyne Ion Tunnels Directing Concentration Redistribution for Commercial-Grade Dendrite-Free Zinc Anodes, *Adv. Mater.* 32 (2020) 2001755.
- [22] R. Zhao, Y. Yang, G. Liu, R. Zhu, J. Huang, Z. Chen, Z. Gao, X. Chen, L. Qie, Redirected Zn Electrodeposition by an Anti-Corrosion Elastic Constraint for Highly Reversible Zn Anodes, *Adv. Funct. Mater.* (2020) 2001867.
- [23] Z.M. Zhao, J.W. Zhao, Z.L. Hu, J.D. Li, J.J. Li, Y.J. Zhang, C. Wang, G.L. Cui, Long-life and deeply rechargeable aqueous Zn anodes enabled by a multifunctional brightener-inspired interphase, *Energy Environ. Sci.* 12 (2019) 1938–1949.
- [24] S. Park, I. Kristanto, G.Y. Jung, D.B. Ahn, K. Jeong, S.K. Kwak, S.-Y. Lee, A single-ion conducting covalent organic framework for aqueous rechargeable Zn-ion batteries, *Chem. Sci.* 11 (2020) 11692–11698.
- [25] M. Winter, B. Barnett, K. Xu, Before Li Ion Batteries, *Chem. Rev.* 118 (2018) 11433–11456.
- [26] K. Xu, Nonaqueous Liquid Electrolytes for Lithium-Based Rechargeable Batteries, *Chem. Rev.* 104 (2004) 4303–4418.
- [27] Q. Wang, D. O'Hare, Recent Advances in the Synthesis and Application of Layered Double Hydroxide (LDH) Nanosheets, *Chem. Rev.* 112 (2012) 4124–4155.
- [28] F. Wang, Z. Guo, In-situ growth of durable superhydrophobic Mg-Al layered double hydroxides nanoplatelets on aluminum alloys for corrosion resistance, *J. Alloys Compd.* 767 (2018) 382–391.
- [29] M.J. Anjum, J. Zhao, V. Zahedi Asl, G. Yasin, W. Wang, S. Wei, Z. Zhao, W. Qamar Khan, In-situ intercalation of 8-hydroxyquinoline in Mg-Al LDH coating to improve the corrosion resistance of AZ31, *Corros. Sci.* 157 (2019) 1–10.
- [30] F. Peng, H. Li, D. Wang, P. Tian, Y. Tian, G. Yuan, D. Xu, X. Liu, Enhanced Corrosion Resistance and Biocompatibility of Magnesium Alloy by Mg-Al-Layered Double Hydroxide, *ACS Appl. Mater. Interfaces* 8 (2016) 35033–35044.
- [31] R.Y. Wang, D.W. Kirk, G.X. Zhang, Effects of Deposition Conditions on the Morphology of Zinc Deposits from Alkaline Zincate Solutions, *J. Electrochem. Soc.* 153 (2006) C357.
- [32] G. Trejo, H. Ruiz, R.O. Borges, Y. Meas, Influence of polyethoxylated additives on zinc electrodeposition from acidic solutions, *J. Appl. Electrochem.* 31 (2001) 685–692.
- [33] C.J. Lan, C.Y. Lee, T.S. Chin, Tetra-alkyl ammonium hydroxides as inhibitors of Zn dendrite in Zn-based secondary batteries, *Electrochim. Acta* 52 (2007) 5407–5416.
- [34] J.C. Ballesteros, P. Díaz-Arista, Y. Meas, R. Ortega, G. Trejo, Zinc electrodeposition in the presence of polyethylene glycol 20000, *Electrochim. Acta* 52 (2007) 3686–3696.
- [35] J.W. Diggle, A. Damjanovic, The Inhibition of the Dendritic Electrococrystallization of Zinc from Doped Alkaline Zincate Solutions, *J. Electrochem. Soc.* 119 (1972) 1649.
- [36] L. Su, L. Liu, B. Liu, J. Meng, X. Yan, Revealing the Impact of Oxygen Dissolved in Electrolytes on Aqueous Zinc-Ion Batteries, *Iscience* 23 (2020) 100995.
- [37] J. Hao, B. Li, X. Li, X. Zeng, S. Zhang, F. Yang, S. Liu, D. Li, C. Wu, Z. Guo, An In-Depth Study of Zn Metal Surface Chemistry for Advanced Aqueous Zn-Ion Batteries, *Adv. Mater.* 32 (2020) 2003021.
- [38] R. Anbarasan, W.D. Lee, S.S. Im, Adsorption and intercalation of anionic surfactants onto layered double hydroxides - XRD study, *Bull. Mater. Sci.* 28 (2005) 145–149.
- [39] P. Zhai, L. Liu, X. Gu, T. Wang, Y. Gong, Interface Engineering for Lithium Metal Anodes in Liquid Electrolyte, *Adv. Energy Mater.* 10 (2020) 2001257.
- [40] W. Liu, P. Liu, D. Mitlin, Review of Emerging Concepts in SEI Analysis and Artificial SEI Membranes for Lithium, Sodium, and Potassium Metal Battery Anodes, *Adv. Energy Mater.* 10 (2020) 2002297.
- [41] T. Wang, N. Zhao, C. Shi, L. Ma, F. He, C. He, J. Li, E. Liu, Interface and Doping Effects on Li Ion Storage Behavior of Graphene/Li₂O, *J. Phys. Chem. C* 121 (2017) 19559–19567.
- [42] T. Wu, K. Zhu, C. Qin, K. Huang, Unraveling the role of structural water in bilayer V2O5 during Zn²⁺-intercalation: insights from DFT calculations, *J. Mater. Chem. A* 7 (2019) 5612–5620.
- [43] J. Shin, D.S. Choi, H.J. Lee, Y. Jung, J.W. Choi, Hydrated Intercalation for High-Performance Aqueous Zinc Ion Batteries, *Adv. Energy Mater.* 9 (2019) 1900083.
- [44] Z. Li, Y. Ren, L. Mo, C. Liu, K. Hsu, Y. Ding, X. Zhang, X. Li, L. Hu, D. Ji, G. Cao, Impacts of Oxygen Vacancies on Zinc Ion Intercalation in VO₂, *ACS Nano* 14 (2020) 5581–5589.
- [45] J.S. Park, J.H. Jo, Y. Aniskevich, A. Bakavets, G. Ragoisha, E. Streletsov, J. Kim, S.T. Myung, Open-Structured Vanadium Dioxide as an Intercalation Host for Zn Ions: Investigation by First-Principles Calculation and Experiments, *Chem. Mater.* 30 (2018) 6777–6787.
- [46] K.W. Nam, H. Kim, J.H. Choi, J.W. Choi, Crystal water for high performance layered manganese oxide cathodes in aqueous rechargeable zinc batteries, *Energy Environ. Sci.* 12 (2019) 1999–2009.
- [47] W. Li, K. Wang, S. Cheng, K. Jiang, An Ultrastable Presodiated Titanium Disulfide Anode for Aqueous "Rocking-Chair" Zinc Ion Battery, *Adv. Energy Mater.* 9 (2019) 1900993.
- [48] X. Yang, W. Deng, M. Chen, Y. Wang, C.-F. Sun, Mass-Producible, Quasi-Zero-Strain, Lattice-Water-Rich Inorganic Open-Frameworks for Ultrafast-Charging and Long-Cycling Zinc-Ion Batteries, *Adv. Mater.* 32 (2020) 2003592.
- [49] Z. Wu, C. Lu, Y. Wang, L. Zhang, L. Jiang, W. Tian, C. Cai, Q. Gu, Z. Sun, L. Hu, Ultrathin VSe(2)Nanosheets with Fast Ion Diffusion and Robust Structural Stability for Rechargeable Zinc-Ion Battery Cathode, *Small* 16 (2020) 2000698.
- [50] W. Yang, L. Dong, W. Yang, C. Xu, G. Shao, G. Wang, 3D Oxygen-Defective Potassium Vanadate/Carbon Nanoribbon Networks as High-Performance Cathodes for Aqueous Zinc-Ion Batteries, *Small Methods* 4 (2020) 1900670.
- [51] Y. Inaguma, C. Liquan, M. Itoh, T. Nakamura, T. Uchida, H. Ikuta, M. Wakihara, High ionic conductivity in lithium lanthanum titanate, *Solid State Commun.* 86 (1993) 689–693.
- [52] H. Buschmann, J. Dölle, S. Berendts, A. Kuhn, P. Bottke, M. Wilkening, P. Heitjans, A. Senyshyn, H. Ehrenberg, A. Lotnyk, V. Duppel, L. Kienle, J. Janek, Structure and dynamics of the fast lithium ion conductor "Li₇La₃Zr₂O₁₂", *PCCP* 13 (2011) 19378–19392.
- [53] R. Kanno, T. Hata, Y. Kawamoto, M. Irie, Synthesis of a new lithium ionic conductor, thio-LISICON-lithium germanium sulfide system, *Solid State Ionics* 130 (2000) 97–104.
- [54] X. Yu, J.B. Bates, G.E. Jellison, F.X. Hart, A Stable Thin-Film Lithium Electrolyte: lithium Phosphorus Oxynitride, *J. Electrochem. Soc.* 144 (1997) 524–532.
- [55] J. Gao, X. Xie, S. Liang, B. Lu, J. Zhou, Inorganic Colloidal Electrolyte for Highly Robust Zinc-Ion Batteries, *Nano-Micro Lett.* 13 (2021) 69.
- [56] L. Ma, S. Chen, X. Li, A. Chen, B. Dong, C. Zhi, Liquid-Free All-Solid-State Zinc Batteries and Encapsulation-Free Flexible Batteries Enabled by In Situ Constructed Polymer Electrolyte, *Angew. Chem.* 132 (2020) 24044–24052.
- [57] W. Liu, D. Lin, A. Pei, Y. Cui, Stabilizing Lithium Metal Anodes by Uniform Li-Ion Flux Distribution in Nanochannel Confinement, *J. Am. Chem. Soc.* 138 (2016) 15443–15450.
- [58] T. Barudžija, N. Cvjetićanin, D. Bajuk-Bogdanović, M. Mojović, M. Mitić, Vibrational and electron paramagnetic resonance spectroscopic studies of β -MnO₂ and α -K MnO₂ nanorods, *J. Alloys Compd.* 728 (2017) 259–270.
- [59] S. Ma, X. Ye, X. Jiang, W. Cen, W. Jiang, H. Wang, First principles calculation of mechanical, dynamical and thermodynamic properties of MnO₂ with four crystal phases, *J. Alloys Compd.* 852 (2021) 157007.
- [60] S. Cheng, L. Yang, D. Chen, X. Ji, Z.-j.J. Jiang, D. Ding, M. Liu, Phase evolution of an alpha MnO₂ -based electrode for pseudo-capacitors probed by in operando Raman spectroscopy, *Nano Energy* 9 (2014) 161–167.